Reduced-Order Modeling of Low Mach Number Unsteady Microchannel Flows

Leila Issa[1]
Department of Mathematics,
Lebanese American University,
Beirut 1102 2801, Lebanon
e-mail: leila.issa@lau.edu.lb

Issam Lakkis
Department of Mechanical Engineering,
American University of Beirut,
Beirut 1107 2020, Lebanon
e-mail: issam.lakkis@aub.edu.lb

We present reduced-order models of unsteady low-Mach-number ideal gas flows in two-dimensional rectangular microchannels subject to first-order slip-boundary conditions. The pressure and density are related by a polytropic process, allowing for isothermal or isentropic flow assumptions. The Navier–Stokes equations are simplified using low-Mach-number expansions of the pressure and velocity fields. Up to first order, this approximation results in a system that is subject to no-slip condition at the solid boundary. The second-order system satisfies the slip-boundary conditions. The resulting equations and the subsequent pressure-flow-rate relationships enable modeling the flow using analog circuit components. The accuracy of the proposed models is investigated for steady and unsteady flows in a two-dimensional channel for different values of Mach and Knudsen numbers. [DOI: 10.1115/1.4026199]

1 Introduction

Early interest in microflows originated in attempts to model the airways in the respiratory system. More recently, with the advent of microelectromechanical systems, modeling gas microflows gained importance in many applications, such as microcompressors, microvalves, microfilters, microcombustors [1], microturbines [2], microthrusters, and micronozzles. The dynamic role of gas surrounding an oscillating microstructure [3] is also an important part in designing robust devices, such as micro-RF switches and resonators. The complexity of these devices makes simulation of the detailed physics an expensive and a time-consuming task. Alternative design and analysis approaches based on reduced-order modeling [4] are attractive due to the advantages they offer in terms of speed, cost, and ability to perform analysis and design in an integrated multiple-domain "circuit design" environment. System-level modeling also enables fast sweeping of the design parameters, thereby reducing significantly the design space. Development of efficient yet accurate reduced-order models for individual components, such as microchannels, is paramount to the viability of system-level design approach.

Microchannels are the most common building blocks of microfluidic devices. They offer transport of small volumes of the working fluid. As opposed to macroscale flows, gaseous microflows are generally laminar with small but significant value of Reynolds number. In some applications, such as microturbomachines [5], Reynolds number could reach a few thousands, indicating the increasing role of inertia effects. Unlike the case with macroscale flows, microgas flows can experience rarefaction (even at a small value of Mach number) when the device's dimensions become comparable to the mean free path of the gas (Knudsen number larger than 0.001). If the departure from continuum is not significant (Kn ≤ 0.1), the Navier–Stokes equations are still applicable with slip-boundary condition [6–8] at a solid wall.

Because of large surface-to-volume ratio of microdevices, it is reasonable to assume that the flow is isothermal if the channel wall is a good heat conductor, such as silicon [7]. Reduced-order dynamic modeling of microchannel isothermal gas flows requires capturing the unsteady behavior of the flow accurately. This is particularly important in applications in which precise control of

the flow conditions is required. For low-inertia isothermal gas flows in large aspect ratio channels ($\alpha \ll 1$, $\mathrm{Re} \ll 1$, and $\mathrm{ReSt} \ll 1$), pressure drop balances the shear force, resulting in the well-known pressure-flow rate relation [7]

$$Q = \frac{h^3}{12\mu}\left(-\frac{\partial p}{\partial x}\right)\left(1 + 6\frac{2-\sigma_v}{\sigma_v}\mathrm{Kn}_0\frac{p_0}{p}\right) \qquad (1)$$

where the subscript zero refers to conditions at the reference temperature T_0. The analog circuit model, shown in Fig. 1, corresponds to a voltage-controlled resistor $R = \frac{12\mu}{h^3}\left(1 + 6\frac{2-\sigma_v}{\sigma_v}\mathrm{Kn}_0\frac{p_0}{p}\right)^{-1}$ per unit length, where the volume flow rate is taken as the through variable (current) and the pressure is taken as the across variable (voltage).

Most models available in the literature account for *steady* isothermal gas flow through parallel channels [9–13]. Those models are either numerical or analytical and they range from slightly compressible [13] to compressible subsonic flows [14]: a numerical investigation of steady isothermal gas flows is presented in Ref. [9], whereas the authors in Ref. [14] present an analytical model based on Burnett momentum equation of a steady isothermal, compressible subsonic gas flow in a microchannel with slowly varying cross section. An analytic and experimental investigation into two-dimensional steady gaseous flow with slight rarefaction through long microchannels is presented in Ref. [10]. The model is based on the Navier–Stokes equations with a first-order slip-velocity boundary condition. Analytical solutions for the pressure and the velocity profiles in a microchannel, derived from the quasigas dynamic equations (QGD), are presented for two-dimensional isothermal steady gas flow in Ref. [12].

A steady subsonic pressure–driven isothermal gas flow in a circular and planar microchannel within the slip-flow regime is studied theoretically in Ref. [15] using a perturbation expansion in Knudsen number and ratio of height to length to solve the compressible Navier–Stokes equations. In particular, it is proven that the isothermal flow assumption is indeed reliable for relatively lower-order expansions. Another solution of a steady isothermal, compressible, and laminar gas flow in either a circular or a planar microchannel with slip boundary conditions that is based on perturbation expansions is presented in Ref. [16]. An analytic solution, based on perturbation in fluid compressibility, to the vorticity-stream function form of the hydrodynamics equations is found for steady laminar weakly compressible isothermal and is presented in Ref. [13]. The authors in Ref. [17] extend the work in
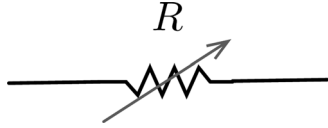
Fig. 1   Inertia-free isothermal model

Ref. [10] by presenting two different sets of asymptotic solutions based on estimations of Reynolds and Mach number at the outlet. The models are presented for steady laminar compressible micro-channel gas flows with a relaxation of the widely used isothermal assumption.

None of the solutions in the aforementioned studies is assimilated in a circuit model, but most importantly, none of them deals with unsteady flows. A system-level circuit model for an *unsteady* incompressible flow in channels of slightly varying cross section is presented in Ref. [18]. The current work can be viewed as an extension of Refs. [19] and [18], where the objective is to present a novel dynamic analog circuit model for low Mach number gas flow undergoing a general polytropic process, where isothermal and isentropic flows are special cases. We consider two-dimensional long channels, where inertia effects are not negligible ($\alpha \ll 1$, Re_hSt_h not necessarily < 1, and αRe_h not necessarily <1). The derived models are compared to the inertia-free model of Eq. (1) and numerical results from computational fluid dynamics (CFD) simulations using ANSYS (FLUENT).

This manuscript is organized as follows: in the first section, the governing equations in dimensionless form for a polytropic flow satisfying the first-order slip boundary condition at the channel's wall are presented. We show in Sec. 2 the expansion of the thermodynamics fields as perturbation series in terms of the low Mach number. This approximation results, up to first order, in a system that satisfies the no-slip boundary condition. The higher-order system satisfies the slip condition at the channel's wall. In Sec. 3, the reduced-order model of these systems is introduced as well as a circuit model for the first-order system. In Sec. 4, the model is validated by numerical simulations, and comparison with FLUENT is shown.

2   Governing Equations in Dimensionless Form for a Polytropic Flow

The conservation of mass and momentum for a single-species nonreacting Newtonian fluid are governed by the following equations [20]:

$$\frac{\partial \rho}{\partial t} + \nabla \cdot (\rho\vec{u}) = 0 \tag{2}$$

$$\rho\left(\frac{\partial \vec{u}}{\partial t} + \vec{u} \cdot \nabla\vec{u}\right) = -\nabla p + \mu\left(\Delta\vec{u} + \frac{1}{3}\nabla(\nabla \cdot \vec{u})\right) \tag{3}$$

where the gravity body force is neglected, as is typical in micro-flows. In these equations, ρ is the density, $\vec{u}$ is the velocity, p is the pressure, and μ is the viscosity of the fluid. The working fluid is assumed to be an ideal gas obeying $p = \rho RT$. We further assume that the pressure and temperature are related by the poly-tropic equation

$$\frac{p}{\rho^l} = \text{constant} \tag{4}$$

which allows for a range of processes, including isothermal and isentropic flow approximations. Here, l is the polytropic constant and $0 < l \leq \gamma$.

We consider gas flow in a channel with width much larger than depth ($w \gg h$) so that the flow can be modeled as two dimensional in the $x - y$ plane, where x refers to the flow direction and y to the transversal direction. The channel cross-sectional area is

assumed to be slowly varying so that $\beta = dh/dx \ll 1$ (in the later, we will consider that $\beta = 0$). We also consider channels with aspect ratios satisfying the condition $\alpha = h_0/L \ll 1$, where L and h_0 are, respectively, the channel length and average depth.

2.1   Nondimensionalization. The governing equations are next presented in dimensionless form to get some insight into the relative scaling of the various physical terms. For that purpose, we introduce the following dimensional quantities with which to scale (here, we use the tilde for the dimensionless variables and the underscore zero for the reference dimensional quantities; for example, $\tilde{p} = p/p_0$)

(1) length scales: $x \sim L$, $y \sim h_0$
(2) velocity $u \sim u_0$, $v \sim v_0 = \beta u_0$ (The continuity equation may be used to come up with appropriate scaling of the y-component of the velocity)
(3) pressure and density: $p \sim p_0$, $\rho \sim \rho_0$
(4) time scale: $t \sim 1/f$, where f is a characteristic forcing frequency

We write the dimensionless version of these equations in component form after dropping the tildes and neglecting terms of order α^2, $\alpha\beta$, and higher. The governing equations for mass continuity and momentum become

$$\text{St}_h\frac{\partial p^{1/l}}{\partial t} + \alpha\frac{(\partial p^{1/l}u)}{\partial x} + \beta\frac{(\partial p^{1/l}v)}{\partial y} = 0 \tag{5}$$

$$\text{Re}_hp^{1/l}\left[\text{St}_h\frac{\partial u}{\partial t} + \alpha u\frac{\partial u}{\partial x} + \beta v\frac{\partial u}{\partial y}\right] = -\alpha\frac{\text{Re}_h}{\gamma\text{Ma}^2}\frac{\partial p}{\partial x} + \frac{\partial^2 u}{\partial y^2} \tag{6}$$

$$\beta\text{Re}_hp^{1/l}\left[\text{St}_h\frac{\partial v}{\partial t}\right] = -\frac{\text{Re}_h}{\gamma\text{Ma}^2}\frac{\partial p}{\partial y} + \beta\frac{\partial^2 v}{\partial y^2} + \frac{1}{3}\frac{\partial}{\partial y}\left(\alpha\frac{\partial u}{\partial x} + \beta\frac{\partial v}{\partial y}\right) \tag{7}$$

where Reynolds, Strouhal, Mach, and Knudsen numbers are, respectively, $\text{Re}_h = \frac{\rho_0 u_0 h_0}{\mu}$, $\text{St}_h = \frac{fh_0}{u_0}$, $\text{Ma} = \frac{u_0}{\sqrt{\gamma RT}}$, and $\text{Kn} = \frac{\lambda}{h_0}$. It should be noted that Kn, Ma, and Re_h are related according to $\text{Kn} = \sqrt{\frac{\gamma\pi\,\text{Ma}}{2\,\text{Re}_h}}$. Note also that the density is replaced by the pressure upon employing the polytropic relation $p = \rho^l$.

2.2   Parallel Channel Flow. The parallel channel flow corresponds to $\beta = 0$ (or $v = 0$) and $h(x) = h_0$, so that the equations for conservation of mass and momentum become

$$\text{St}_h\frac{\partial p^{1/l}}{\partial t} + \alpha\frac{\partial}{\partial x}(p^{1/l}u) = 0 \tag{8}$$

$$\text{Re}_hp^{1/l}\left[\text{St}_h\frac{\partial u}{\partial t} + \alpha u\frac{\partial u}{\partial x}\right] = -\alpha\frac{\text{Re}_h}{\gamma\text{Ma}^2}\frac{\partial p}{\partial x} + \frac{\partial^2 u}{\partial y^2} \tag{9}$$

$$-\frac{\text{Re}_h}{\gamma\text{Ma}^2}\frac{\partial p}{\partial y} + \frac{\alpha}{3}\frac{\partial}{\partial y}\left(\frac{\partial u}{\partial x}\right) = 0 \tag{10}$$

These equations are subject to first-order slip boundary condition at the wall and symmetry condition at the centerline

$$u\big|_{y=1/2} = -\frac{2-\sigma_v}{\sigma_v}\frac{\text{Kn}}{p^{1/l}}\frac{\partial u}{\partial y}\bigg|_{y=h/2} \quad \text{and} \quad \frac{\partial u}{\partial y}\bigg|_{y=0} = 0 \tag{11}$$

3   The Low-Mach-Number Approximation

In the low-Mach-number model [21], the pressure is decomposed into a dynamic component, p_1, and thermodynamic component, p_0, the ratio of which is O(Ma^2). This enables decoupling the density and pressure so that the total pressure may be replaced everywhere by the thermodynamic pressure, except in the momentum equation. As such, density variations in an ideal gas arise

only from temperature variations according to $p_0 = \rho RT$. Large-amplitude density and temperature fluctuations are therefore allowed, and the only requirement is that the total pressure stays close to the background pressure p_0, which is nearly constant for open domains but is generally time dependent in closed domains, such as channels. So we consider flows for which Mach number is a small parameter that we denote by $\varepsilon = \sqrt{\gamma}\text{Ma} \ll 1$, which means that the velocity field and other quantities should be rescaled accordingly.

We now seek expansions in ε. It should be noted that the first-order slip-boundary condition is a valid assumption [7] for $\text{Kn} < 0.1$. It is then justifiable to assume $\text{Kn} = O(\varepsilon)$, although the discussion that follows will be also valid for $\text{Kn} = O(\varepsilon^q), 1 \leq q < 2$. So we shall write $\text{Kn} = A\varepsilon$, where A is some order one constant. This enables expansion of the slip-boundary condition in terms of ε. Since $\text{Kn} = \sqrt{\pi/2}(\varepsilon/\text{Re}_h)$, it follows that Re_h is $O(1)$ or larger. We further make the assumption that the channel's aspect ratio α is also a small parameter on the order of ε, i.e., $\alpha = B\varepsilon$, where B is some order one constant.

With these assumptions, the resulting system for conservation of mass and momentum (Eqs. (8)–(10)) is

$$\text{St}_h \frac{\partial p^{1/l}}{\partial t} + B\varepsilon \frac{\partial}{\partial x}(p^{1/l}u) = 0 \tag{12}$$

$$\varepsilon p^{1/l}\left(\text{St}_h \frac{\partial u}{\partial t} + B\varepsilon u \frac{\partial u}{\partial x}\right) = -B\frac{\partial p}{\partial x} + \frac{A}{\sqrt{\pi/2}}\varepsilon \frac{\partial^2 u}{\partial y^2} \tag{13}$$

$$-\sqrt{\frac{\pi}{2}}\frac{\partial p}{\partial y} + \frac{B\varepsilon^3}{3}\frac{\partial}{\partial y}\left(\frac{\partial u}{\partial x}\right) = 0 \tag{14}$$

where the boundary conditions at the solid wall and the centerline are, respectively,

$$(p^{1/l}u)\big|_{y=1/2} = -\frac{2-\sigma_v}{\sigma_v}A\varepsilon\frac{\partial u}{\partial y}\bigg|_{y=1/2} \quad \text{and} \quad \frac{\partial u}{\partial y}\bigg|_{y=0} = 0 \tag{15}$$

We now seek a perturbation expansion of the velocity and pressure fields as follows:

$$p = p_0 + \varepsilon p_1 + \varepsilon^2 p_2 + O(\varepsilon^3)$$
$$u = u_0 + \varepsilon u_1 + \varepsilon^2 u_2 + O(\varepsilon^3) \tag{16}$$

$$v = v_0 + \varepsilon v_1 + \varepsilon^2 v_2 + O(\varepsilon^3) \tag{17}$$

We also use the approximation

$$p^{1/l} \sim (p_0 + \varepsilon p_1 + \varepsilon^2 p_2)^{1/l} \sim p_0^{1/l}\left(1 + \frac{1}{l}\varepsilon p_1/p_0 + \frac{1}{l}\varepsilon^2 p_2/p_0\right) \tag{18}$$

The expansions result in two systems of equations, the first of which combines $O(\varepsilon^0)$ and $O(\varepsilon)$ and relates the zeroth-order velocity to the first-order pressure,

$$\text{System 1}\begin{cases} \dfrac{\partial p_0}{\partial t} = 0 & (19) \\[2mm] \dfrac{\partial p_0}{\partial t} = 0 & (20) \\[2mm] \dfrac{\partial p_0}{\partial y} = 0 & (21) \\[2mm] \dfrac{\text{St}_h}{l p_0}\dfrac{\partial p_1}{\partial t} + B\dfrac{\partial u_0}{\partial x} = 0 & (22) \\[2mm] p_0^{1/l}\text{St}_h \dfrac{\partial u_0}{\partial t} = -B\dfrac{\partial p_1}{\partial x} + \dfrac{A}{\sqrt{\pi/2}}\dfrac{\partial^2 u_0}{\partial y^2} & (23) \end{cases}$$

satisfying the no-slip boundary condition at the solid wall in addition to the symmetry condition at the centerline

$$u_0\big|_{y=1/2} = 0 \quad \text{and} \quad \frac{\partial u_0}{\partial y}\bigg|_{y=0} = 0 \tag{24}$$

The second system of equations combines $O(\varepsilon)$ and $O(\varepsilon^2)$ and relates the first-order velocity to the second order-pressure

$$\text{System 2}\begin{cases} \dfrac{\text{St}_h}{l p_0}\dfrac{\partial p_2}{\partial t} + B\left(\dfrac{\partial u_1}{\partial x} + \dfrac{1}{l p_0}\dfrac{\partial p_1 u_0}{\partial x}\right) = 0 & (25) \\[3mm] p_0^{1/l}\left(\text{St}_h\left(\dfrac{p_1}{l p_0}\dfrac{\partial u_0}{\partial t} + \dfrac{\partial u_1}{\partial t}\right) + B u_0\dfrac{\partial u_0}{\partial x}\right) = -B\dfrac{\partial p_2}{\partial x} + \dfrac{A}{\sqrt{\pi/2}}\dfrac{\partial^2 u_1}{\partial y^2} & (26) \end{cases}$$

satisfying the *slip*-boundary condition at the solid wall in addition to the symmetry condition at the centerline

$$p_0^{1/l}\left(u_1 + \frac{p_1}{l p_0}u_0\right)_{y=1/2} = -\frac{2-\sigma_v}{\sigma_v}A\frac{\partial u_2}{\partial y}\bigg|_{y=1/2} \quad \text{and} \quad \frac{\partial u_1}{\partial y}\bigg|_{y=0} = 0 \tag{27}$$

Since the y-momentum equation in Eq. (14) is $O(\varepsilon^3)$, it can be inferred that the pressure does not depend on the transversal direction (to the order we are considering).

3.1 The Reduced-Order Model for the First-Order System.
We are going to solve the first system now. It is clear from the momentum equations in Eqs. (19)–(21) that the zeroth-order pressure field is a constant $p_0(x, y, t) \equiv p_0$. The momentum equation of the next order Eq. (23) is viewed as a diffusion equation for the zeroth-order velocity field $u_0(x, y, t)$, with a forcing term consisting of the first-order pressure $p_1(x, t)$.

Our solution approach for this equation uses the integral transform in the transversal variable y defined as

$$\hat{u}(x, \beta_m, t) = \int_0^{1/2} \mathcal{K}(\beta_m, y')u_0(x, y', t)dy' \tag{28}$$

along with the inverse transform

$$u_0(x, y, t) = \sum_{m=0}^{\infty} \mathcal{K}(\beta_m, y)\hat{u}(x, \beta_m, t) \tag{29}$$

where the kernel solves the eigenvalue problem

$$\frac{d^2\phi}{dy^2} + \beta^2\phi(y) = 0 \quad \text{in} \quad 0 \leq y \leq 1/2 \tag{30}$$

subject to the boundary condition

$$\phi'(0) = 0 \quad \text{and} \quad \phi(1/2) = 0 \qquad (31)$$

The solution of Eq. (30) is

$$\mathcal{K}(\beta_m, y) = 2\cos\beta_m y \qquad (32)$$

where β_m solves the characteristic equation

$$\cos\beta_m/2 = 0 \Rightarrow \beta_m = (2m+1)\pi, \quad m = 0, 1, \cdots \qquad (33)$$

Note that the norm of the kernel is defined as

$$N_m = \int_0^{1/2} \mathcal{K}(\beta_m, y)dy = \frac{(-1)^m}{(m+1/2)\pi} \qquad (34)$$

Applying this transform to Eq. (23), we obtain

$$\mathrm{St}_h p_0^{1/l} \frac{\partial \hat{u}}{\partial t} = -BN_m \frac{\partial p_1}{\partial x} - \frac{A}{\sqrt{\pi/2}} \beta_m^2 \hat{u} \qquad (35)$$

with the initial condition $\hat{u}(x, t = 0) = 0$, which is solved to get

$$\hat{u}(x, \beta_m, t) = -\frac{B}{\mathrm{St}_h p_0^{1/l}} N_m \int_0^t \frac{\partial p_1(x,s)}{\partial x} e^{-\frac{A\beta_m^2}{\sqrt{\pi/2}p_0^{1/l}\mathrm{St}_h}(t-s)} ds \qquad (36)$$

Inverting the transform, we get

$$u_0(x,y,t) = -\frac{B}{\mathrm{St}_h p_0^{1/l}} \sum_m N_m \mathcal{K}_m(y) \int_0^t \frac{\partial p_1(x,s)}{\partial x} e^{-\frac{A\beta_m^2}{\sqrt{\pi/2}p_0^{1/l}\mathrm{St}_h}(t-s)} ds \qquad (37)$$

where β_m satisfies the characteristic equation in Eq. (33) and the kernel is given by Eq. (32).

Upon integrating in y, we get the volume flow rate

$$Q_0(x,t) = -\frac{2B}{\mathrm{St}_h p_0^{1/l}} \sum_m N_m^2 \int_0^t \frac{\partial p_1(x,s)}{\partial x} e^{-\frac{A\beta_m^2}{\sqrt{\pi/2}p_0^{1/l}\mathrm{St}_h}(t-s)} ds \qquad (38)$$

and integrating x, we get the average volume flow rate between inlet and outlet,

$$\overline{Q}(t) = \int_0^1 Q(x,t)dx = \sum_m \overline{Q}_m(t) \qquad (39)$$

where

$$\overline{Q}_m(t) = \frac{2B}{p_0^{1/l}\mathrm{St}_h\varepsilon} N_m^2 \int_0^t \Delta p(s) e^{-\frac{A\beta_m^2}{\sqrt{\pi/2}p_0^{1/l}\mathrm{St}_h}(t-s)} ds \qquad (40)$$

It can be seen that the average mass flow rate $\overline{Q}_m(t)$ satisfies

$$\varepsilon \frac{\mathrm{St}_h p_0^{1/l}}{2BN_m^2} \frac{d\overline{Q}_m}{dt} + \varepsilon \frac{A\beta_m^2}{2\sqrt{\pi/2}BN_m^2} \overline{Q}_m = \Delta p \qquad (41)$$

which corresponds to the circuit model shown in Fig. 2. The circuit is made up of an infinite number of parallel branches, with
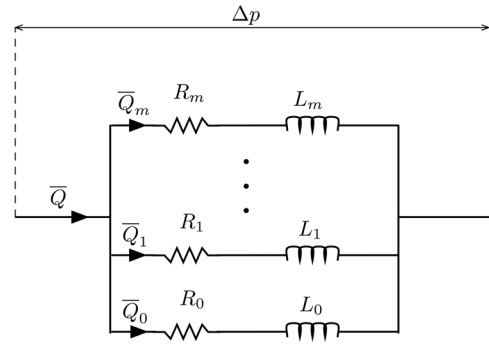
Fig. 2 Circuit model

each branch consisting of an inductance L_m in series with a resistance R_m, where

$$L_m = \varepsilon \frac{\mathrm{St}_h p_0^{1/l}}{2BN_m^2} \qquad (42)$$

$$R_m = \varepsilon \frac{A\beta_m^2}{2\sqrt{\pi/2}BN_m^2} \qquad (43)$$

Note that the steady solution for a constant Δp, obtained from Eq. (40) by taking the limit $t \to \infty$, reduces to the classical Poiseuille solution

$$\overline{Q}^{steady} = \frac{B\mathrm{Re}_h\Delta p}{12\varepsilon} \qquad (44)$$

3.2 The First-Order Pressure Distribution. An equation for the first-order pressure profile is derived here. Upon combining the derivative of Eq. (38) with respect to x and the mass equation of Eq. (22), a partial differential equation (PDE) for the first-order pressure $p_1(x,t)$ is obtained,

$$\frac{\partial p_1}{\partial t} = \frac{2B^2}{\mathrm{St}_h^2} l(p_0)^{1-1/l} \sum_{m=0}^{\infty} N_m^2 \int_0^t \frac{\partial^2 p_1}{\partial x^2}(x,s) e^{-\frac{A\beta_m^2}{\sqrt{\pi/2}p_0^{1/l}\mathrm{St}_h}(t-s)} ds \qquad (45)$$

where $0 \le x \le 1$. The pressure satisfies the initial condition $p_1(x, t = 0)$ and the inhomogeneous boundary conditions

$$p_1(x = 0, t) = p_1^{in}(t) \quad p_1(x = 1, t) = p_1^{out}(t) \qquad (46)$$

We shall now solve this PDE for the pressure. Using the transformation

$$p_1(x,t) = \mathcal{P}_1(x,t) + p_1^{in}(t) + (p_1^{out}(t) - p_1^{in}(t))x \qquad (47)$$

$\mathcal{P}_1$ is then governed by

$$\frac{\partial \mathcal{P}_1}{\partial t} + \frac{dp_1^{in}}{dt} + x\frac{d(p_1^{out} - p_1^{in})}{dt} = \frac{2B^2}{\mathrm{St}_h^2} l(p_0)^{1-1/l}$$
$$\times \sum_{m=0}^{\infty} N_m^2 \int_0^t \frac{\partial^2 \mathcal{P}_1(x,s)}{\partial x^2} e^{-\frac{A\beta_m^2}{\sqrt{\pi/2}p_0^{1/l}\mathrm{St}_h}(t-s)} ds \qquad (48)$$

with the initial condition $\mathcal{P}_1(x, t = 0) = p_1(x, 0) - p_1^{in}(0) - (p_1^{out}(0) - p_1^{in}(0))x$ and subject to the homogenous boundary conditions $\mathcal{P}_1(x = 0, t) = 0 \quad \mathcal{P}_1(x = 1, t) = 0$. Equation (48) is solved with the aid of spatial transforms. Let us define the spatial transform in the flow direction x along with the inverse transform, respectively, as

$$\hat{\mathcal{P}}_1(\lambda_n, t) = \int_0^1 \tilde{\mathcal{K}}(\lambda_n, x')\mathcal{P}_1(x', t)dx' \tag{49}$$

$$\mathcal{P}_1(x, t) = \sum_{n=0}^{\infty} \tilde{\mathcal{K}}(\lambda_n, x)\hat{\mathcal{P}}_1(\lambda_n, t) \tag{50}$$

where the kernel solves the eigenvalue problem

$$\frac{d^2\phi}{dx^2} + \lambda^2\phi(x) = 0 \quad \text{in} \quad 0 \leq x \leq 1 \tag{51}$$

subject to the boundary condition $\phi(0) = 0$ and $\phi(1) = 0$. The solution of Eq. (51) is

$$\tilde{\mathcal{K}}(\lambda_n, x) = \sqrt{2}\sin\lambda_n x \quad \text{and} \quad \sin\lambda_n = 0 \Rightarrow \lambda_n = n\pi, \quad n = 1, 2, \cdots \tag{52}$$

After applying this transform on the PDE for $\mathcal{P}_1$, an ordinary differential equation (ODE) for $\hat{\mathcal{P}}_1$ is obtained

$$\frac{d\hat{\mathcal{P}}_1}{dt}(\lambda_n, t) + \frac{dp_1^{\text{in}}}{dt}M_n^0 + \frac{d(p_1^{\text{out}} - p_1^{\text{in}})}{dt}M_n^1$$
$$= -\lambda_n^2 \frac{2B^2}{\text{St}_h^2}l(p_0)^{1-1/l}\sum_{m=0}^{\infty}N_m^2\int_0^t \hat{\mathcal{P}}_1(\lambda_n, s)e^{-\frac{A\beta_m^2}{\sqrt{\pi/2}p_0^{1/l}\text{St}_h}(t-s)}ds \tag{53}$$

with the initial condition $\hat{\mathcal{P}}_1(\lambda_n, t = 0) = \hat{p}_1(\lambda_n, 0) - p_1^{\text{in}}(0)M_n^0 - (p_1^{\text{out}}(0) - p_1^{\text{in}}(0))M_n^1$. The moments of the Kernel are

$$M_n^0 = \int_0^1 \tilde{\mathcal{K}}(\lambda_n, x)dx = \frac{\sqrt{2}}{n\pi}(1 - (-1)^n) \quad \text{and}$$

$$M_n^1 = \int_0^1 x\tilde{\mathcal{K}}(\lambda_n, x)dx = \sqrt{2}\frac{(-1)^{n+1}}{n\pi}, \quad n = 1, 2, \cdots \tag{54}$$

With this in hand, we can solve the ODE for $\hat{\mathcal{P}}_1$, then invert the transform using Eq. (50), and then obtain $p_1(x, t)$ using Eq. (47). Once we have the first-order pressure profile, we can get the zeroth-order velocity and mass flow rate.

3.3 The Reduced-Order Model for the Second-Order System.
We are now ready to solve the higher-order system Eqs. (25) and (26). We shall use a very similar methodology to Sec. 3.2, so we will be concise in the exposition.

This system obviously depends on the solution of the first order system in Secs. 3.1–3.2. Before proceeding, let us define the following *known* quantities that depend on the previous solutions u_0, p_1, and p_0:

(1) $\Psi(x, t) = \dfrac{B}{lp_0}\dfrac{\partial(p_1 Q_0)}{\partial x}$

(2) $g(x, t) = -\dfrac{2 - \sigma_v}{\sigma_v}A\dfrac{\partial u_0}{\partial y}(x, y = 1/2, t)$

(3) $F(x, y, t) = -\dfrac{p_0^{1/l}}{lp_0}\text{St}_h p_1\dfrac{\partial u_0}{\partial t} - p_0^{1/l}Bu_0\dfrac{\partial u_0}{\partial x} - \text{St}_h\dfrac{\partial g}{\partial t}$

Also, define the transformation

$$\tilde{u}_1(x, y, t) = u_1(x, y, t) - g(x, t) \tag{55}$$

that yields the PDE

$$p_0^{1/l}\text{St}_h\frac{\partial\tilde{u}_1}{\partial t} = \frac{A}{\sqrt{\pi/2}}\frac{\partial^2\tilde{u}_1}{\partial y^2} - B\frac{\partial p_2}{\partial x} + F(x, y, t) \tag{56}$$

with homogeneous boundary conditions

$$\frac{\partial\tilde{u}_1}{\partial y}(x, y = 0, t) = 0, \quad \tilde{u}_1(x, y = 1/2, t) = 0 \tag{57}$$

We view this equation as a diffusion equation for the first-order velocity u_1 with a forcing term that is driven by two components: the first is $F(x, y, t)$, the term accounting for the previous system, and the second is the second-order pressure field.

Using the same technique as in Sec. 3.2, we solve for the first-order pressure field and obtain

$$u_1(x, y, t) = \frac{1}{\text{St}_h p_0^{1/l}}\sum_m \mathcal{K}_m(y)\int_0^t e^{-\frac{A\beta_m^2}{\sqrt{\pi/2}(p^0)^{1/l}\text{St}_h}(t-s)}$$
$$\times \left[-BN_m\frac{\partial p^2(x, s)}{\partial x} + \hat{F}_m(x, s)\right]ds + g(x, t) \tag{58}$$

where β_m satisfies the characteristic equation in Eq. (33) and the kernel is given by Eq. (32).

As for the mass flow rate, it is given by

$$Q_1(x, t) = \frac{2}{\text{St}_h p_0^{1/l}}\sum_m N_m\int_0^t e^{-\frac{A\beta_m^2}{\sqrt{\pi/2}p_0^{1/l}\text{St}_h}(t-s)}$$
$$\times \left[-BN_m\frac{\partial p_2(x, s)}{\partial x} + \hat{F}_m(x, s)\right]ds + g(x, t) \tag{59}$$

In a similar way to the methodology used for solving the first system, we obtain a PDE for the second-order pressure profile

$$\frac{\partial p_2}{\partial t}(x, t) = \frac{2lB^2(p_0)^{1-1/l}}{\text{St}_h^2}$$
$$\times \sum_m N_m^2\int_0^t e^{-\frac{A\beta_m^2}{\sqrt{\pi/2}p_0^{1/l}\text{St}_h}(t-s)}\frac{\partial^2 p_2(x, s)}{\partial x^2}ds + S(x, t) \tag{60}$$

where the source term $S(x, t)$ is given by

$$S(x, t) = g(x, t) - \frac{lp_0}{\text{St}_h}\Psi(x, t) - \frac{lp_0 B}{\text{St}_h}\frac{\partial g}{\partial x}(x, t)$$
$$-\frac{2lB(p_0)^{1-1/l}}{\text{St}_h^2}\sum_m N_m\times\int_0^t e^{-\frac{A\beta_m^2}{\sqrt{\pi/2}p_0^{1/l}\text{St}_h}(t-s)}\hat{F}_m(x, s)ds \tag{61}$$

It should be noted that the hat in the above equation refers to the transform in the transversal direction y, defined in Sec. 3.1.

4 Model Validation and Discussion

The model shown in Fig. 2 enables system-level analysis of channel flow using the conventional techniques employed in circuit analysis. Direct current (DC) analysis is steady-state analysis in which the transient term is set to zero and all the inductors in Fig. 2 are short circuited. Transient analysis can also be performed by integrating the ODEs in time using circuit simulation tools, such as SPICE.

Accuracy and performance of our model presented in Sec. 3.3 are addressed in terms of steady and transient isothermal flow of air in the channel depicted in Fig. 3 for different operating conditions. The channel length and height are, respectively, 2000 μm and 20 μm. The channel is preceded by an entry section in order for the flow to reach fully developed conditions at the inlet to the main section. The boundary condition at the inlet of the entry section is prescribed in terms of time-varying inlet mass flux $(\rho_i V_i)$,
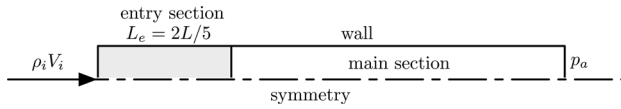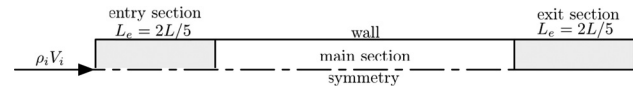
Fig. 3 Schematic for first set of simulations

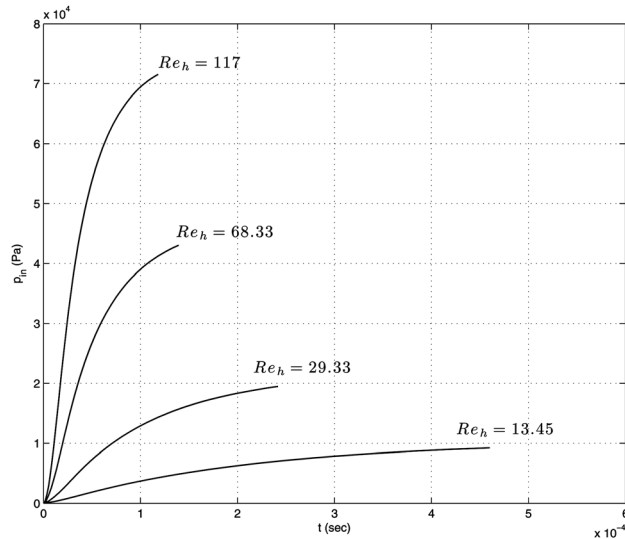**Fig. 6 Schematic for second set of simulations**

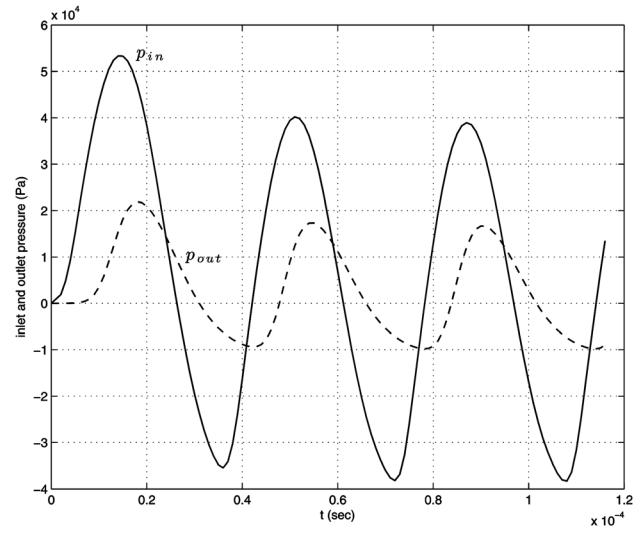**Fig. 4 Pressure at inlet to main section for set 1**

Fig. 7 Pressure at inlet (——) and outlet (- - -) of main section versus time (CFD)
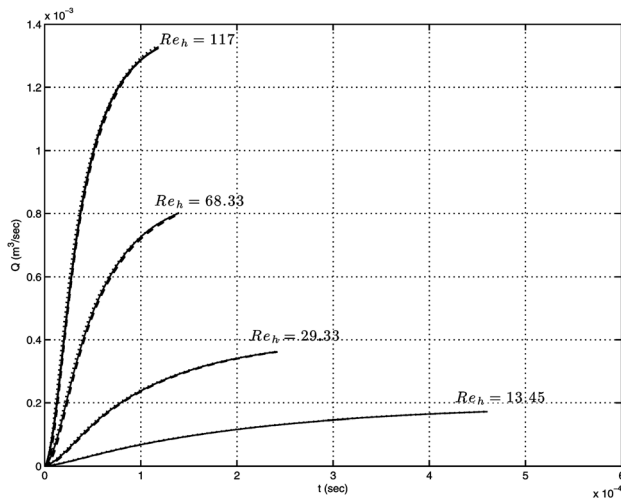

Fig. 5 Average volume flow rate predicted by the model (- - - -) compared with FLUENT (——)
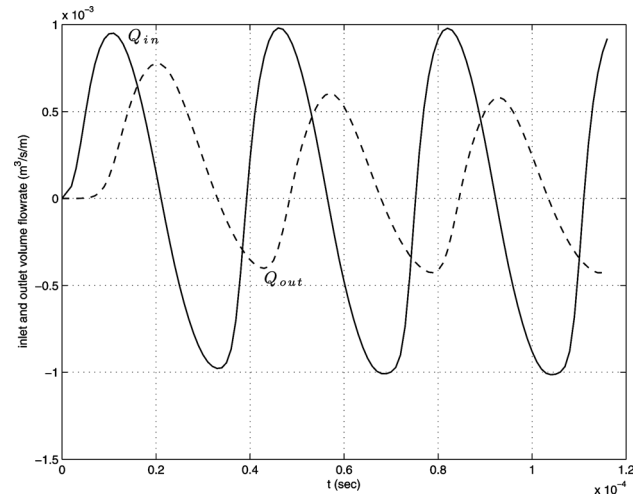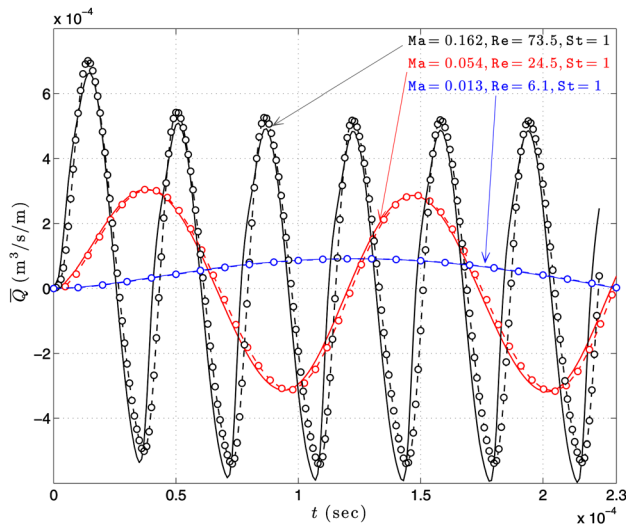

Fig. 8 Volume flow rate at inlet (——) and outlet (- - -) of main section versus time (CFD)

assumed to be spatially uniform. At the outlet of the main section, atmospheric pressure is prescribed.

In the first set of simulations, $\rho_i V_i = (\rho_i V_i)_{\max}(1 - \exp(-t/\tau))$, where $\tau = L/V_{i,\max}$. The values of Reynolds number corresponding to $V_{i,\max}$ are, respectively, 13.45, 29.3, 68.3, and 117. For each case, the pressure history at the inlet of the main section ($p_i(t)$), shown in Fig. 4, is recorded from the CFD (FLUENT) transient simulation. $p_i(t)$ is then used as input to the model in order to compute the corresponding time-varying mean volume flow rate. The volume flow rate computed from the reduced-order model is in good agreement with that obtained from CFD (FLUENT), as shown in Fig. 5.

In the second set, the mass flux at the entry section inlet is given a prescribed harmonic time variation according to $\rho_i V_i = (\rho_i V_i)_{\max} \sin(2\pi f t)$, where the frequency is chosen according to $f^{-1} = L/V_{i,\max}$ so that $\text{St} = 1$. For this set of simulations, another section is added to the outlet of the main section with length of $2L/5$, as depicted in Fig. 6. Three cases are considered (i) $\text{Ma} = 0.013, \text{Re} = 6.1$; (ii) $\text{Ma} = 0.054, \text{Re} = 24.5$; and (iii) $\text{Ma} = 0.162, \text{Re} = 73.5$. For all three cases, $\text{Kn} = 0.0032$, which implies that the no-slip condition at solid boundary holds. For each case, the pressure history at the inlet and outlets of the main section ($p_i(t)$ and $p_o(t)$), shown in Fig. 7 for case (iii), is recorded from the CFD (FLUENT) transient simulation. $p_i(t)$ and $p_o(t)$ are then used as input to our model in order to compute the corresponding time-varying flow rate along the channel. The inlet, outlet, and average volume flow rates predicted by the model for these pressure profiles are compared with those obtained from FLUENT, such as those presented in Fig. 8 for case (iii).
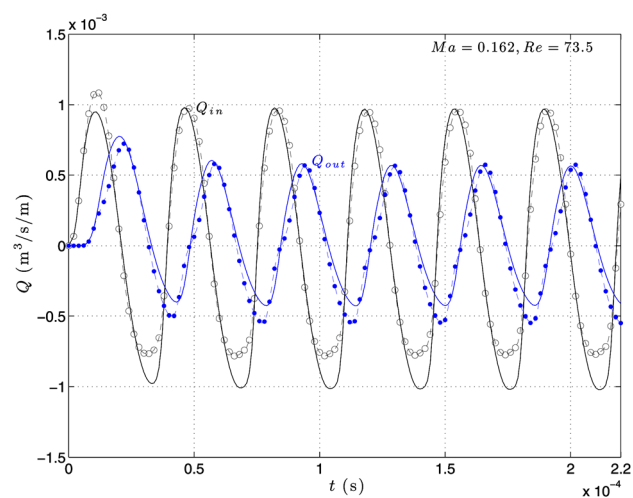
Fig. 9 Comparison of time evolution of mean volume-flow rate between model (- -o- -) and CFD (——) for different values of Mach number
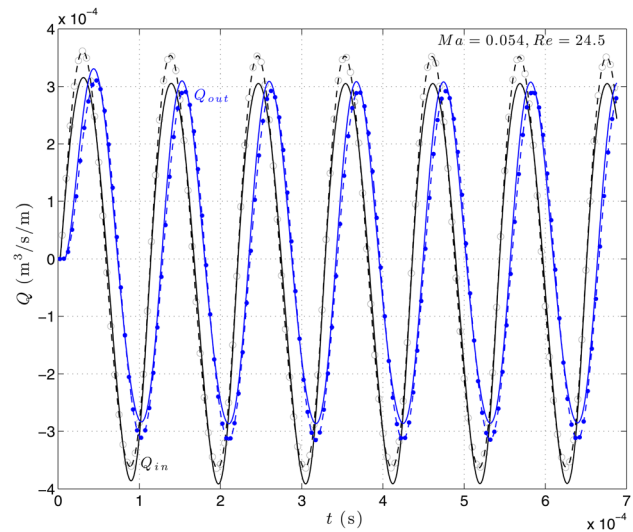
Fig. 11 Comparison of time evolution of inlet and outlet volume-flow rates between model (- -o- -) and CFD (——) for case (ii)
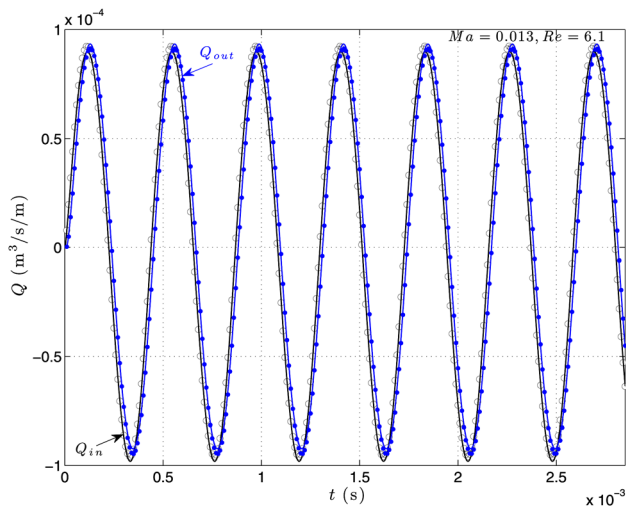
Fig. 10 Comparison of time evolution of inlet and outlet volume-flow rates between model (- -o- -) and CFD (——) for case (i)

Fig. 12 Comparison of time evolution of inlet and outlet volume-flow rates between model (- -o- -) and CFD (——) for case (iii)

Time evolution of the mean volume flow rate is plotted in Fig. 9, where the numerical (CFD) solution is compared to that predicted by the proposed model for the three cases (i) $Ma = 0.013, Re = 6.1$; (ii) $Ma = 0.054, Re = 24.5$; and (iii) $Ma = 0.162, Re = 73.5$. It can be observed from Fig. 9 that the model yields more accurate results at smaller values of Mach and Reynolds number, as inferred by the agreement with the CFD solution. This is expected because the model is developed for low-Mach-number flows. It should be noted that the simulation time using the model is a very small fraction of that of the CFD simulation tool. For example, the ratio of the model simulation time to the CFD simulation time for the case $Ma = 0.054, Re = 24.5$ is 1/280.

Time evolution of the volume flow rate at channel inlet and outlet predicted by the model is compared to those obtained from CFD simulations in Figs. 10, 11, and 12 for cases (i), (ii), and (iii), respectively. It can be observed that the inlet and outlet volume flow rate are close to each other for small values of Ma and move farther apart for larger values of Ma. This is expected since, at lower Mach number values, the flow is closer to the incompressible

Table 1 % Relative error between model and CFD

	$\varepsilon = \sqrt{\gamma}\mathrm{Ma}$	$\overline{Q}$	Q_{in}	Q_{out}
case (i)	0.0158	1.7%	2.7%	2.56%
case (ii)	0.0635	8%	11.5%	12.6%
case (iii)	0.2	32%	19%	37%

limit and is unable to store additional mass inside the channel by compressing the gas. Incompressibility causes inlet and outlet volume flow rate to be close to each other in terms of magnitude and phase, as shown in Fig. 10 for case (i), where $Ma = 0.013$. For larger values of Mach number, compressibility endows the flow with the ability to store mass inside the channel, rendering inlet and outlet volume flow rates different from each other both in terms of magnitude and phase, as shown in Fig. 12 for case (iii), where $Ma = 0.162$. It can be observed that the model captures these variations in magnitude as well as phase for both inlet and outlet volume flow rates. The relative errors, measured as the L2 norm of the difference between inlet, outlet, and average
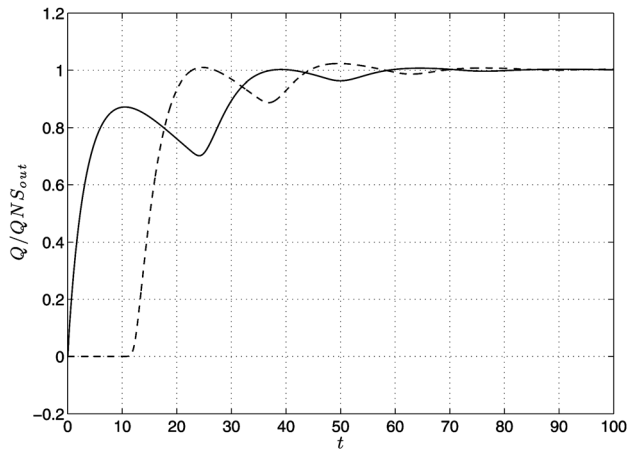
Fig. 13 Time evolution of inlet (———) and outlet (- - -) volume-flow rates. Kn = **0.00216.**
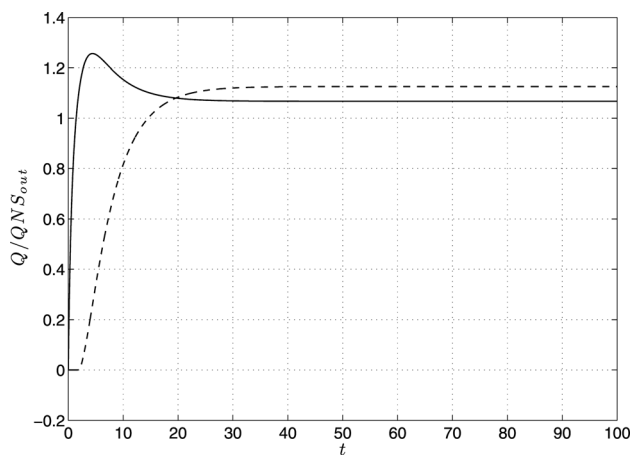

Fig. 14 Time evolution of inlet (———) and outlet (- - -) volume flow rates. Kn = **0.013.**

volume flow rate predicted by the model and those obtained from CFD simulations, over the entire time period, are presented in Table 1 for cases (i), (ii), and (iii).

In the last set of cases, we present the impact of slip on the volume flow rates at inlet and outlet of channel. In this set of simulations, the channel aspect ratio was fixed at $h/L = 0.01$. The inlet pressure is increased from 100 kPa to 130 kPa according to $p_{in}(t) = 100 + 30(1 - e^{-t/\tau})$, where $\tau = h/U$, U being the average velocity at steady state and no-slip conditions at boundary. The outlet pressure is kept at 100 kPa. The channel width h is varied from $2\mu m$ to $30\mu m$ so that Kn covers the range $[0.002 - 0.032]$. Time response of the inlet and outlet volume flow rates (normalized by the steady outlet volume flow rate at no-slip condition) to the applied pressure is presented in Fig. 13 for the case where Kn = 0.00216. This is essentially a no-slip case, which explains why both flow rates settle to the steady no-slip value. The wavy behavior is attributed to the relatively high inertia Re = 83 and to the effect of compressibility (Ma = 0.12), which is also responsible for the phase shift between the inlet and outlet volume flow rate. Figure 14 presents a case where Kn = 0.013, Re = 2.3, and Ma = 0.02. The effect of slip condition at the solid boundary is apparent as the volume flow rates settle at values higher than the steady no-slip case. In this case, the ratios of the volume flow rate to the no-slip volume flow rate is 1.067, which is in good agreement with the inertia-free first-order slip solution [7] $Q/Q_{ns} = 1 + 12(2 - \sigma_v/\sigma_v)(Kn_o/p_{in}/p_{out} + 1)$. In this case, $\sigma_v = 1$ and $p_{in}/p_{out} = 1.3$ at steady state.

5 Conclusion

Reduced-order models for unsteady low-Mach-number polytopic flow of an ideal gas in a two-dimensional parallel channel are presented for no-slip as well as first-order slip-boundary conditions. To first order (in Mach number), the model that satisfies the no-slip condition at solid boundaries can be represented as an analog electric circuit consisting of a set of parallel branches, each consisting of a resistance and an inductor in series. The resistors model viscous dissipation and the inductors correspond to inertia due to the time-varying term. The model can also include higher-order effects, which account for first-order slip condition at solid boundaries. The accuracy and validity of the proposed model are investigated in terms of the dynamic response of the volume flow rate for sinusoidal as well as step-function pressure history. The proposed model offers a tradeoff between speed and accuracy, which is possible by controlling the number of parallel branches included in the model.

Acknowledgment

Nomenclature

A = channel cross-sectional area
f = characteristic forcing frequency
h = height of rectangular channel cross section
Kn = Knudsen number
L = channel length
Ma = Mach number
p = pressure
Q = volume flow rate
R = ideal gas constant
Re_h = Reynolds number based on channel's height
St_h = Strouhal number based on channel's height
t = time
u = velocity component in flow direction
$\vec{u}$ = velocity vector
x = coordinate in flow direction
y = coordinate along channel height
α = channel aspect ratio (h/L)
γ = ratio of constant pressure to constant volume-specific heat
λ = mean free path
μ = dynamic viscosity
ρ = density
σ_v = accommodation coefficient

References

[1] Shan, X., Wang, Z., Jin, Y., Wu, M., Hua, J., Wong, C., and Maeda, R., 2005, "Studies on a Micro Combustor for Gas Turbine Engines," J. Micromech. Microeng., **15**(9), p. S215–S221.
[2] Isomura, K., Murayama, M., Teramoto, S., Hikichi, K., Endo, Y., Togo, S., and Tanaka, S., 2006, "Experimental Verification of the Feasibility of a 100 W Class Micro-scale Gas Turbine at an Impeller Diameter of 10 mm," J. Micromech. Microeng., **16**(9), p. S254–S261.
[3] Diab, N., and Lakkis, I., 2012, "DSMC Simulations of Squeeze Film Between a Micro Beam Undergoing Large Amplitude Oscillations and a Substrate," Proceedings of the ASME 2012 10th International Conference on Nanochannels, Microchannels, and Minichannels, ICNMM2012.
[4] Senturia, S. D., 2001, *Microsystem Design*, Springer, New York.
[5] Epstein, A., 2004, "Millimeter-Scale, Micro-electro-mechanical Systems Gas Turbine Engines," ASME J. Eng. Gas Turbines Power, **126**, p. 205–226.
[6] Maxwell, J., 1879, "On Stresses in Rarified Gases Arising From Inequalities of Temperature," Philos. Trans. R. Soc. London, **170**, pp. 231–256.
[7] Karniadakis, G., Beskok, A., and Aluru, N., 2005, *Microflows and Nanoflows: Fundamentals and Simulation*, Vol. 29, Springer, New York.
[8] Al-Bender, F., Lampaert, V., and Swevers, J., 2005, "The Generalized Maxwell-Slip Model: A Novel Model for Friction Simulation and Compensation," IEEE Trans. Autom. Control, **50**(11), pp. 1883–1887.
[9] Cao, B., Chen, G., Li, Y., and Yuan, Q., 2006, "Numerical Analysis of Isothermal Gaseous Flows in Microchannel," Chem. Eng. Technol., **29**(1), pp. 66–71.

[10] Arkilic, E., Schmidt, M., and Breuer, K., 1997, "Gaseous Slip Flow in Long Microchannels," J. Microelectromech. Syst., **6**(2), pp. 167–178.

[11] Jang, J., and Wereley, S., 2004, "Pressure Distributions of Gaseous Slip Flow in Straight and Uniform Rectangular Microchannels," Microfluid. Nanofluid., **1**(1), pp. 41–51.

[12] Graur, I., Meolans, J., and Zeitoun, D., 2006, "Analytical and Numerical Description for Isothermal Gas Flows in Microchannels," Microfluid. Nanofluid., **2**(1), pp. 64–77.

[13] Venerus, D., and Bugajsky, D., 2010, "Compressible Laminar Flow in a Channel," Phys. Fluids, **22**, p. 046101.

[14] Stevanovic, N., 2007, "A New Analytical Solution of Microchannel Gas Flow," J. Micromech. Microeng., **17**(8), p. 1695–1702.

[15] Qin, F., Sun, D., and Yin, X., 2007, "Perturbation Analysis on Gas Flow in a Straight Microchannel," Phys. Fluids, **19**, p. 027103.

[16] Zohar, Y., Lee, S., Lee, W., Jiang, L., and Tong, P., 2002, "Subsonic Gas Flow in a Straight and Uniform Microchannel," J. Fluid Mech., **472**(1), pp. 125–151.

[17] Cai, C., Sun, Q., and Boyd, I., 2007, "Gas Flows in Microchannels and Microtubes," J. Fluid Mech., **589**(589), pp. 305–314.

[18] Lakkis, I., 2008, "System-Level Modeling of Microflows in Circular and Rectangular Channels," ICNMM2008, ASME.

[19] Issa, L., and Lakkis, I., 2013, "Reduced Order Models of Low Mach Number Isothermal Flows in Microchannels," Proceedings of ICNMM2013 the ASME 2013 11th International Conference on Nanochannels, Microchannels, and Minichannels.

[20] Batchelor, G. K., 2000, *An Introduction to Fluid Dynamics*, Cambridge University, Cambridge, UK.

[21] Majda, A., and Lamb, K. G., 1991, Simplified Equations for Low Mach Number Combustion With Strong Heat Release, Springer, New York.